How to cite: *Angew. Chem. Int. Ed.* **2025**, e202516573
doi.org/10.1002/anie.202516573

Artificial Ion Channels

Chirality-Induced Split Personality in Polymer with Intrinsic Microporosity-Based Artificial Ion Channels

Fei Gou, Zihong Yang, Qiuting Wang, Wenju Chang, Jie Shen, and Huaqiang Zeng*

Abstract: The construction of artificial transmembrane ion channels using polymers has emerged as a promising research avenue in membrane transport. In this study, we have designed and synthesized an intriguing class of intrinsically microporous chiral polyimides (PIM-PIs) employing *trans*/*cis*-1,2-diaminocyclohexanes (DACH) as structural building blocks. Remarkably, these chiral PIM-PIs exhibit distinct configurations, leading to contrasting ion transport properties. The cis-DACH-derived chiral polymer **1** demonstrates the hitherto highest Li^+ transport activity (>100 pS), along with exceptionally high selectivity ratios for Li^+/Na^+ (17.1) and Li^+/K^+ (21.8). In contrast, chiral polymers **2a** and **2b**, synthesized from (1*R*,2*R*)-DACH and (1*S*,2*S*)-DACH, respectively, showcase pronounced anion transport capabilities and a remarkably high Cl^-/K^+ selectivity ratio of 17.6. This work introduces a multifunctional, chiral PIM-based artificial ion channel system with a "split personality" governed by its chiral constituents. It represents the first application of chiral polymers in transmembrane transport, inspiring innovative design strategies for developing polymer-based artificial ion channels.

The study of artificial transmembrane ion channels spans numerous disciplines, including biology, chemistry, physics, and engineering, driving significant advances in both foundational research and real-world applications.[1–18] By investigating artificial channels, researchers gain deeper insights into biological systems, discovering innovative tools and methods to tackle challenges in modern medicine and environmental science.[19] These studies also help illuminate the structure, function, and regulatory mechanisms of natural ion channels,[20–24] enhancing our understanding of cellular signal transduction, neurotransmission, and electrophysiological processes—knowledge that underpins the creation of new therapeutic approaches. Moreover, artificial ion channels hold tremendous potential for applications in targeted drug delivery, bioengineering, environmental remediation, and nanomaterials. Therefore, developing advanced artificial transmembrane transport systems is not only of great scientific importance but also offers substantial practical benefits across diverse fields.

Compared to diverse types of artificial transmembrane ion channels self-assembled from small molecule,[1–18] polymer-based ion channels have received relatively less attention, yet they hold significant importance in the field. Currently, four types of polymeric backbones have been utilized in constructing ion channels: random sequence polymer systems developed by Xu[25] and Liu,[26,27] bottlebrush polymers with more defined sequences,[28] aromatic foldamer-derived polymeric helices,[29–38] and, more recently, polymers with intrinsic porosity.[39] Designing and developing novel polymer-based therefore artificial transmembrane channel systems presents both significant opportunities and complex challenges.

Polyimide-based polymers with intrinsic microporosity (PIM-PIs) are a class of porous materials distinguished by their unique microporous structures.[40–44] The rigid and contorted structure of PIM building blocks hinders tight packing of polymer chains, resulting in a high free volume and the formation of micropores typically smaller than 2 nm in diameter. Additionally, PIMs are characterized by their exceptional thermal stability, outstanding mechanical properties, and remarkable porosity, making them highly sought after for gas separation and storage applications.[45–48] We recently pioneered the creation of PIM-based artificial transmembrane lithium channels, demonstrating exceptionally high Li^+ transmembrane transport activity, with conduction rate exceeding 40 pS and high transport selectivity factors of >10 over both Na^+ and K^+ ions.[39]

The development of chiral microporous materials is widely regarded as a significant advancement in materials science, spanning diverse areas from scientific research to practical applications.[49–52] The incorporation of chiral motifs into these materials not only disrupts the symmetry of the pore structure, creating channel pathways with distinct chiral properties, but also alters the physicochemical environment within the channels, regulating noncovalent interactions with guest molecules. This unique combination endows chiral pore structures with exceptional selectivity and recognition capabilities for guest molecules.[53–55] For example, such approaches have been extensively explored in metal–organic

[*] Dr. F. Gou, Z. Yang, Q. Wang, Dr. W. Chang, Prof. Dr. J. Shen, Prof. Dr. H. Zeng
College of Chemistry, Fuzhou University, Fuzhou, Fujian 350116, China
E-mail: ShenJie@fzu.edu.cn
Prof. Dr. H. Zeng
State Key Laboratory of Chemistry for NBC Hazards Protection, College of Chemistry, Fuzhou University, Fuzhou, Fujian 350116, China

Additional supporting information can be found online in the Supporting Information section

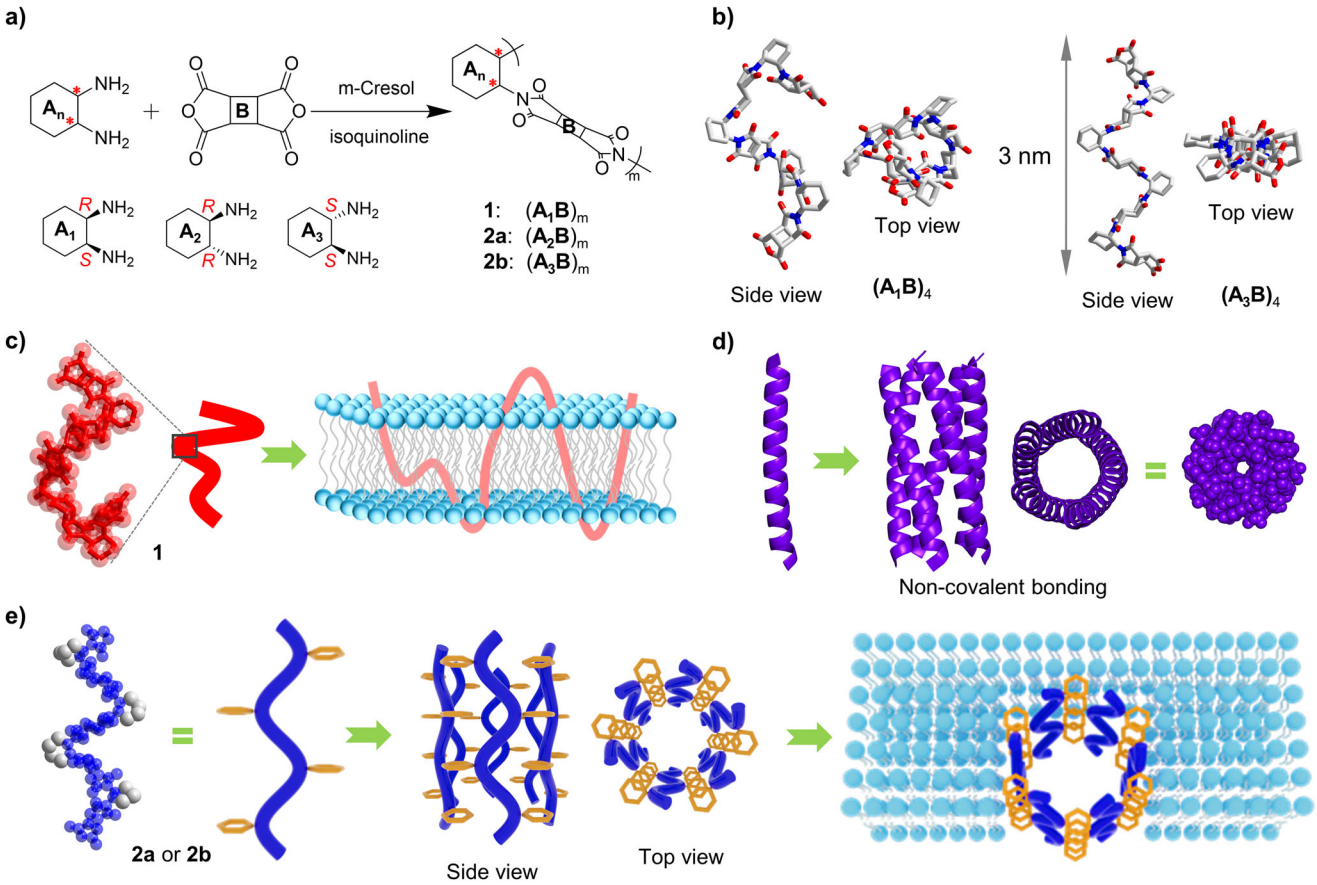

Figure 1. a) One-pot preparation of AB-type chiral PIM-PIs using chiral 1,2-diaminocyclohexanes with different configurations as one of the PIM building blocks. b) Geometrically optimized structures of two tetrameric oligomers at the level of M06-2X/6-31+G(d). c) Schematic representation of **1** embedded within a bilayer membrane, illustrating its role in facilitating ion transport across the membrane through its intrinsic pore. d) Structural diagram of an α-helix and the corresponding α-helix bundle formed through various noncovalent forces within the side chain. e) van der Waals interactions among the one-dimensionally aligned side chains, which may enable **2a** or **2b** to self-assemble, creating a tubular cavity for anion transport. Note that ensembles of varying sizes are also possible, and lipid molecules may participate in the dynamic process of ensemble formation.

frameworks and covalent organic framework, where they play pivotal roles in chiral molecular separation, optical molecular recognition, and chiral catalysis.[55–57]

Therefore, introducing chiral PIM-PI units could provide a promising approach, fostering more diverse design strategies and advancing the development of new PIM-based artificial transmembrane ion channels to broaden their potential applications.

Aligned with this perspective, we propose the incorporation of chiral motifs into the PIM-PI backbone to leverage molecular chirality, thereby modulating its structural configuration and, consequently, its microporous architecture and functionality. This approach could enable the tunable design of PIM-based artificial ion channels with significantly enhanced or distinct transport functions.

Given the widespread commercial availability of three stereoisomers for 1,2-DACH scaffold, we selected them as building blocks to synthesize PIM-PIs, which might have distinctively different frameworks via a straightforward one-pot polymerization method (Figure 1a). Although PIM-PI **1** is composed of meso-monomers (*cis*-DACH), its asymmetric polymeric backbone imparts chirality to its structure. Interestingly, these types of chiral PIMs manifest divergent ion transport properties when embedded in lipid bilayer membranes.

Specifically, chiral polymer **1** exhibits exceptionally high Li^+ transport activity, achieving record-high conduction rates exceeding 100 pS. Additionally, it shows remarkable selectivity, with selectivity factors greater than 17.7 and 21.8 over Na^+ and K^+, respectively, highlighting its superior performance in ion discrimination and transport efficiency.

Nevertheless, chiral polymers **2a** and **2b**, prepared from (*1R*,*2R*)-DACH and (*1S*,*2S*)-DACH, respectively, exhibit high anion transport activity and high selectivity. Particularly, **2b** demonstrates a conductance value of >70 pS, with Cl^-/K^+ selectivity exceeding 17. Hence, we achieve tunable transmembrane transport of both cations and anions within the same DACH-derived PIM-PI frameworks. To the best of our knowledge, this represents the first instance of such a phenomenon.

PIM-PIs **1** and **2** were synthesized using a previously established two-step procedure with minor modifications.[58] *Trans*- or *cis*-DACH (1.00 mmol) and dianhydride (1.00 mmol) were dissolved in 4 mL *m*-cresol under a nitrogen atmosphere and

then sequentially heated to 80 °C for 1 h and to 180 °C for 4 h. Following the reaction, 60 mL MeOH was added to precipitate the crude polymer (Figure 1a and Scheme S1), which was washed and purified twice with 60 mL MeOH. Gel permeation chromatography (GPC) was utilized to determine the molecular weights of the three polymers, each exhibiting a single peak, with molecular weights of 82.9, 142.7, and 133.5 kDa, respectively (Table S1). NMR spectra confirmed the polymeric nature of the compounds, displaying broad signals (Figures S1–S3).

To gain insight into the structural features of these chiral PIM-PIs, we computationally optimized a short segment containing 4.5 repeating $\mathbf{A}_n\mathbf{B}$ units for chiral polymers **1** and **2b** at the level of M06-2X/6-31+G(d). Computational results reveal two distinct types of molecular configurations (Figure 1b). Polymer **1** exhibits a twisted and irregular structure characterized by localized loops and nonuniform conformations, with pronounced asymmetry. Conversely, **2a** and **2b** display a well-ordered structure, with the cyclohexane units projecting outward from the polymer central axis in a staggered manner.

The distinct configurational differences between **1** and **2a** or **2b** strongly indicate that they adopt unique channel structures when embedded in a bilayer membrane, resulting in varied ion transport properties. As illustrated later, these differences are indeed reflected in their ion transport behavior: **1** facilitates cation transport, whereas both **2a** and **2b** predominantly transport anions.

Based on the computed structure and experimentally verified cation transport property, we propose that cations traverse through a network of ion-coordinating functional groups along the polymeric backbone of **1** (Figure 1c). Resembling the structure of an α-helix in terms of backbone and side-chain orientation, **2a** or **2b** may assemble into a barrel-like structure, similar to the formation of an α-helix bundle, where multiple α-helices align side by side through side-chain interactions (Figure 1d).[59] This might result in a sufficiently large pore that facilitates transmembrane anion transport (Figure 1e). This pore-forming strategy has been adopted by several research groups to design pores for facilitated transmembrane anion transport.[60–66]

The ion transport activities of **1**, **2a**, and **2b** were evaluated using a vesicle-based kinetic HPTS assay, which employs a pH-sensitive HPTS dye within a DOPC-based bilayer membrane (Figure 2a). By varying extravesicular alkali metal chlorides MCl (Figure 2a) and normalizing against background values of 8.0%, 6.4%, 6.6%, 3.2%, and 10.1% (Figure S4), we obtained **1**-mediated ion transport activities of 90% (Li^+), 26% (Na^+), 34% (K^+), 27% (Rb^+), and 27% (Cs^+) at 10 μg mL^{-1}, respectively. The data suggest that polymer **1** shows a high preference for Li^+ transport, with weaker yet comparable transport abilities for Na^+, K^+, Rb^+, and Cs^+ ions.

For **2a** and **2b**, varying the extravehicular buffer from LiCl to CsCl leads to insignificant changes in ion transport activity, with transport activities for all ions reaching 60%–70%. This suggests the minimum involvement of alkali metal ions in ion transport (Figure 2a). These findings help exclude the possibility of Na^+/OH^- symport and Na^+/H^+ antiport ion transport mechanisms. Instead, **2a** and **2b** transport either H^+ or Cl^- ions through Cl^-/H^+ symport or Cl^-/OH^- antiport mechanism.

To further investigate the type of species transported, a series of additional experiments were conducted on **2a** and **2b**. As shown in Figure 2b, we conducted the SPQ assay to determine whether Cl^- ions could be transported. SPQ is a Cl^--sensitive dye whose fluorescence is quenched in the presence of Cl^- ions. Upon addition of **2a** or **2b**, we observed rapid quenching of SPQ fluorescence, with Cl^- transport activities reaching 65% and 68%, respectively. This indicates that **2a** or **2b** effectively transports Cl^- ions. Additionally, cation-transporting **1** does not cause significant changes in SPQ fluorescence (Figure 2b), indicating that the chiral building blocks have a determining influence on the polymer's ion transport behavior.

To compare the ion transport rates between Cl^- and H^+ or OH^-, FCCP, a highly active proton transporter, was added to the HPTS assay (Figure 2c). The principle of this assay is that the relatively faster transport of Cl^- anions will lead to the accumulation of H^+ inside the LUVs. FCCP then facilitates the rapid efflux of these accumulated protons, resulting in enhanced HPTS fluorescence intensity and increased ion transport activity. Experimentally, we observed significantly increased transport efficiency for both **2a** and **2b** in the presence of FCCP (from 44% to 52% and from 47% to 56%, respectively). These enhancements suggest a faster transport rate for Cl^- compared to H^+ or OH^-.

We can corroborate the above finding using the same HPTS in the presence of VA, a K^+-selective carrier. It is anticipated that the influx of K^+ mediated by VA would trigger the influx of Cl^- or OH^- to maintain the charge neutrality. If Cl^- transport is the rate-determining step, the addition of VA will restore the suppressed OH^- transport rate, resulting in enhanced HPTS fluorescence intensity. As shown in Figure 2d, the combination of VA (10 pM) with **2a** or **2b** did not result in any cooperative effect, indicating a clear preference for Cl^- transport over OH^- or H^+.

We further conducted a CF dye leakage assay to evaluate the LUV membrane integrity in the presence of **1**, **2a**, and **2b** (Figure 2e). Our results show that while all polymer channels do not induce any fluorescence increase at 10 μg mL^{-1}, the melittin, a pore-forming peptide[67] as the positive control in this assay, causes significant fluorescence increases of 55% and 100% at exceptionally lower concentrations of 5 and 25 nM, respectively. These results unambiguously confirm that the LUV membrane integrity is maintained in the presence of these polymer channels and that the pore formed by these polymers, if any, must be less than 1 nm, which is the size of the CF molecule (Figure S6).

Hill analyses of the vesicle-based kinetic data gave the EC_{50} values of 0.5 μg mL^{-1} for **1** (Figure S5a), 5.0 μg mL^{-1} for **2a** (Figure S5b), and 3.5 μg mL^{-1} for **2b** (Figure S5c), respectively, affirming their high Li^+ and Cl^- transport activities.

The varying assays applying HPTS, SPQ, or CF dyes for both **2a** and **2b** demonstrate a high degree of similarity, indicating comparable ion transport properties (Figure 2). However, their EC_{50} values differ by about 30% (5.0 μg

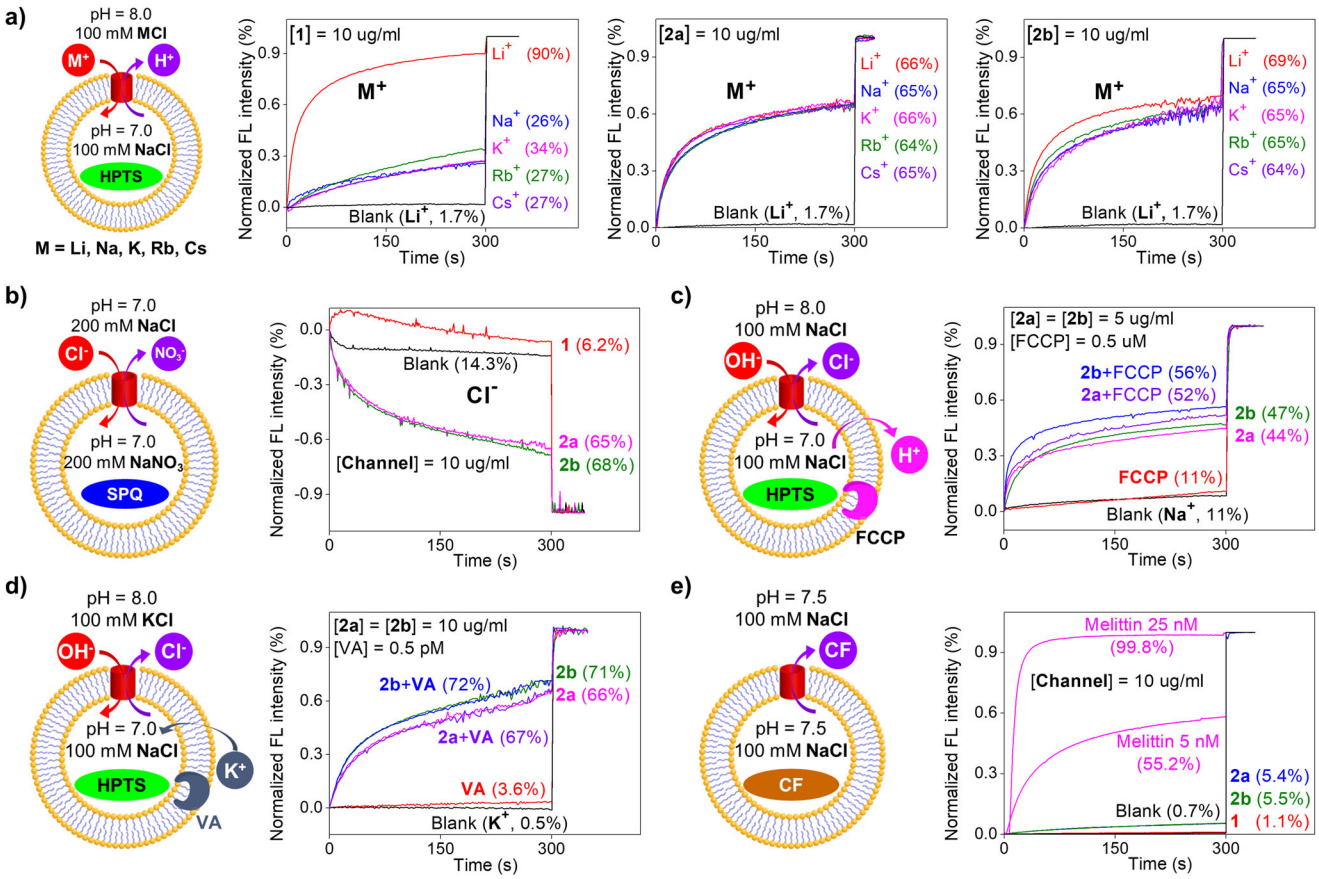

Figure 2. a) Schematic representation of the DOPC-based pH-sensitive HPTS assay for ion transport study of **1**, **2a**, and **2b**, employing different extravesicular salts (MCl, where M = Li, Na, K, Rb, and Cs) to compare ion transport selectivities. b) The chloride-sensitive SPQ assay for assessing the chloride transport capacity of **1**, **2a**, and **2b**. c) The HPTS assay using a proton carrier FCCP to compare the ion transport rate between proton and chloride anion by **2a** and **2b**. d) The HPTS assay using a K^+ carrier VA to compare the ion transport rate between hydroxide and chloride anion by **2a** and **2b**. e) CF dye leakage assay to confirm the membrane integrity in the presence of **1**, **2a**, and **2b**. DOPC = dioleoyl phosphatidylcholine, HPTS = 8-hydroxypyrene-1,3,6-trisulfonic acid trisodium salt, SPQ = (6-methoxy-*N*-(3-sulfopropyl))quinolinium, FCCP = carbonyl cyanide 4-(trifluoromethoxy) phenylhydrazone, VA = valinomycin, CF = 5(6)-carboxy fluorescein.

mL^{-1} for **2a** and 3.5 for **2b**, Figure S5b,c), which may be attributed to differences in molecular weight ($M_n \approx 142.7$ kDa for **2a** and $M_n \approx 133.5$ kDa for **2b**). This variation in polymer length could influence backbone conformation, aggregation propensity, polymer–polymer interactions, and membrane insertion kinetics, ultimately resulting in slight differences in ion transport behavior. To elucidate the ion transport mechanism of **1** and **2**, single-channel electrophysiological experiments were performed in diPhyPC-based planar lipid bilayer membrane using a planar lipid bilayer workstation (Figures 3 and S7). The recorded single-channel current traces for **1** and **2b** indicate that these polymer channels mediate ion transport via a channel mechanism.

Based on the plotted current versus voltage (*I–V*) curves, the conductance rate ($\gamma_{Li}{}^+$) of **1** for transporting Li^+ was calculated to be 104.4 ± 0.4 pS. This value is not only much higher than the previous two cases reported by Dong et al. (27.1 pS) and us (18.4 pS), but also more than twice the $\gamma_{Li}{}^+$ values of our newly developed PIMs-based Li^+ ion channel (42.9 pS). These data confirm that the chiral polymer channel **1** efficiently transports Li^+ ions at a record-high rate. To determine the ion transport selectivity of **1**, single-channel conductance measurements were conducted in asymmetrical baths (Figures 3a and S8, S9). From the plotted *I–V* curves, the reverse potential values were determined to be −73.8 and −79.2 mV, corresponding to Li^+/Na^+ and Li^+/K^+ selectivity factors of 17.7 and 21.8, respectively.

Similar analysis of the *I–V* curve yielded a $\gamma_{Cl}{}^-$ value of 71.8 ± 0.2 pS for **2b**, demonstrating efficient and rapid transport of Cl^- ion. Based on this conductance value, the channel's pore size is estimated to be 6 Å in diameter using the Hille equation.[68] To determine the Cl^-/K^+ transport selectivity, single-channel conductance measurements were performed in asymmetric conditions. From the *I–V* curve (Figure 3c), a reverse potential of −16.0 mV was recorded, leading to a selectivity factor of 17.6 and highlighting a preference for Cl^- transport over K^+.

While our study exclusively focused on polymeric systems, we have also synthesized a short *trans*-oligomer $(\mathbf{A_2B})_4$ composed of four $\mathbf{A_2}$ and three **B** units (Figure S10a) and characterized by ^{1}H NMR (Figure S10b). Crucially, the same HPTS assay demonstrates that this short oligomer exhibits

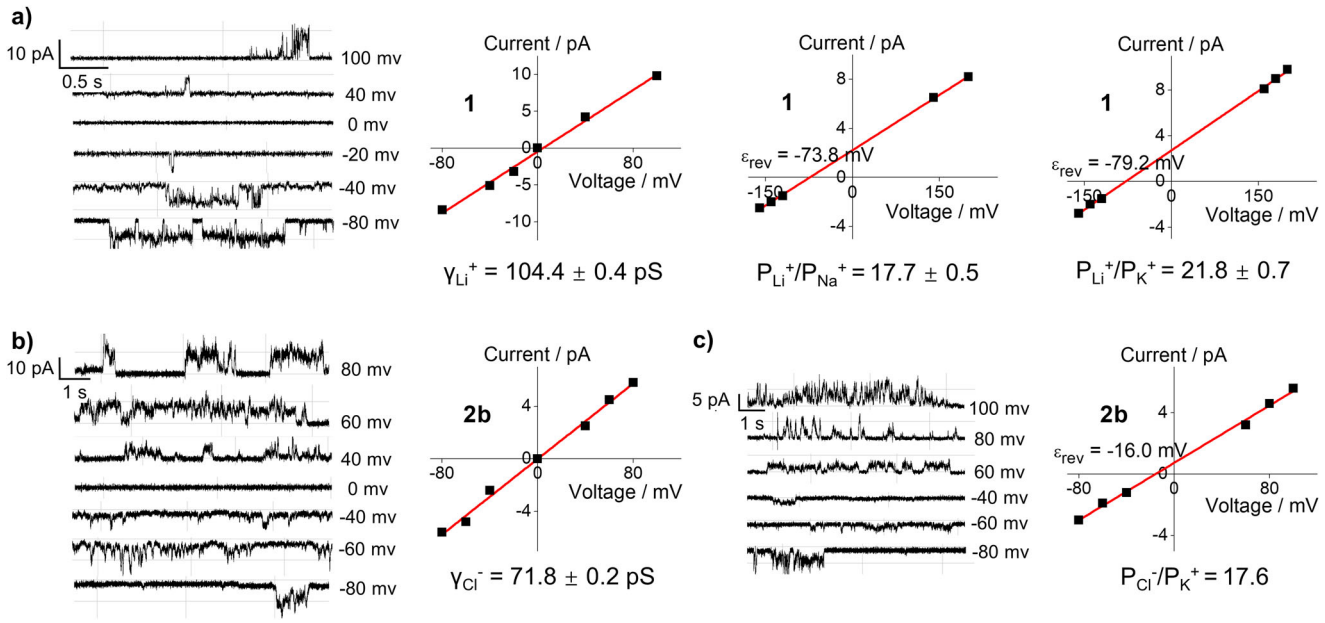

Figure 3. a) Single-channel current traces and current–voltage (*I–V*) curves (*cis* chamber = *trans* chamber = 1 M LiCl) from which lithium conduction rate (γ_{Li}^+) value for **1** was determined to be 104.4 ± 0.4 pS. Displayed on the right are the other two *I–V* curves (*cis* chamber = 1 M LiCl, *trans* chamber = 1 M NaCl or 1 M KCl) from which the selectivity factors of P_{Li}^+/P_{Na}^+ and P_{Li}^+/P_K^+ for **1**-mediated ion transport were determined to be 17.7 and 21.8, respectively. b) Describes single-channel current traces and the corresponding *I–V* curves for **2b** (*cis* chamber = *trans* chamber = 1 M KCl) from which γ_{Cl}^- value was determined to be 71.8 ± 0.2 pS. c) Describes single-channel current traces and the corresponding *I–V* curves for **2b** (*cis* chamber = 0.5 M KCl, *trans* chamber = 1 M KCl) from which the selectivity factor of P_{Cl}^-/P_K^+ for **2b**-mediated transport was determined to be 17.6. Here, γ_{Li}^+ and γ_{Cl}^- values were obtained by fitting the *I–V* curves using a linear equation of $y = a + b*x$ where slope b is γ in the unit of pS. P_{Li}^+/P_M^+ and P_{Cl}^-/P_K^+ values were calculated using a simplified Goldman–Hodgkin–Katz equation $\varepsilon_{rev} = RT/F \times \ln(P_M^+/P_{Li}^+)$ and $\varepsilon_{rev} = RT/F \times \ln\{(P_K^+[K^+]_{trans} + P_{Cl}^-[Cl^-]_{cis})/(P_K^+[K^+]_{cis} + P_{Cl}^-[Cl^-]_{trans})\}$, respectively, where R = universal gas constant (8.314 J K^{-1} mol^{-1}), T = 298 K, F = Faraday's constant (96485 C mol^{-1}), and P is the ion permeability. All single-channel current traces were recorded in a diPhyPC-based bilayer membrane. diPhyPC = 1,2-diphytanoyl-sn-glycero-3-phosphocholine.

no significant ion transport activity (Figure S10c), consistent with our hypothesis that functional ion channels require supramolecular assembly of polymers with a longer backbone.

Given the significant differences in ion transport observed among chiral polymers, we have conducted a series of theoretical calculations to investigate this phenomenon. However, due to computational constraints (e.g., system size, timescales), modeling entire polymers in explicit lipid membranes remains prohibitively challenging. Moreover, a single polymer chain may adopt a significantly different conformation by interacting with other polymer molecules or when embedded within a membrane. Therefore, our approach leverages complementary methods—density function theory (DFT) at the M06-2X/6-31+G(d) level and semi-empirical method-based conformational search at the GFN2-xTB level—to identify low-energy conformations of oligomeric structures such as $(\mathbf{A_1B})_4$ and $(\mathbf{A_3B})_4$, each containing four $\mathbf{A_1}$ units and five **B** units to serve as proxies for local polymer behavior.

For *cis*-polymer channel **1**, as illustrated in Figure S11, we first systematically investigated the binding energies between short segments, which contain one or two $\mathbf{A_1B}$ repeating units, and the Li^+ ion hydrated with up to three water molecules, i.e., $\mathbf{A_1B}{\bullet}Li^+{\bullet}(H_2O)_3$, $\mathbf{A_1B}{\bullet}Li^+{\bullet}(H_2O)_2$ and $(\mathbf{A_1B})_2{\bullet}Li^+$). The binding energies for $\mathbf{A_1B}{\bullet}Li^+{\bullet}(H_2O)_2$ and $(\mathbf{A_1B})_2{\bullet}Li^+$ were calculated to be 8.3 and 9.1 kcal mol^{-1}, respectively, suggesting that the combined effects of metal coordination and hydrogen bonding between polyimide carbonyl oxygens, Li^+, and water molecules are insufficient to overcome the energy required for dehydration, specifically the removal of two or four water molecules from lithium ions. In contrast, $\mathbf{A_1B}{\bullet}Li^+{\bullet}(H_2O)_3$ has a binding energy of -7.1 kcal mol^{-1}, indicating that the removal of one water molecule is energetically favorable. Therefore, we propose that lithium ion transport likely occurs primarily in a trihydrated state, with polyimide carbonyl oxygen atoms providing the driving forces. In addition, through combined DFT calculation at the M06-2X/6-31+G(d) level and conformational search at the GFN2-xTB level (Figure S12a), we determined that the short segment of polymer **1**, i.e., structure of $(\mathbf{A_1B})_4$, adopts a relatively disordered and loose conformation, possibly mediating Li^+ transport across the membrane through interactions with polyimide carbonyl oxygen atoms.

For *trans*-polymer channels **2a** or **2b**, both DFT calculation at the M06-2X/6-31+G(d) level and conformational search at the GFN2-xTB level reveal that the short-segment structure of $(\mathbf{A_3B})_4$ possesses a relatively more ordered conformation, with the cyclohexyl moieties distributing relatively orderly along both sides of the polyimide backbone (Figure S12b). Drawing an analogy to nature, where pore-forming peptides/proteins insert into membranes to form functional channels, diverse pore-forming artificial membrane transporters

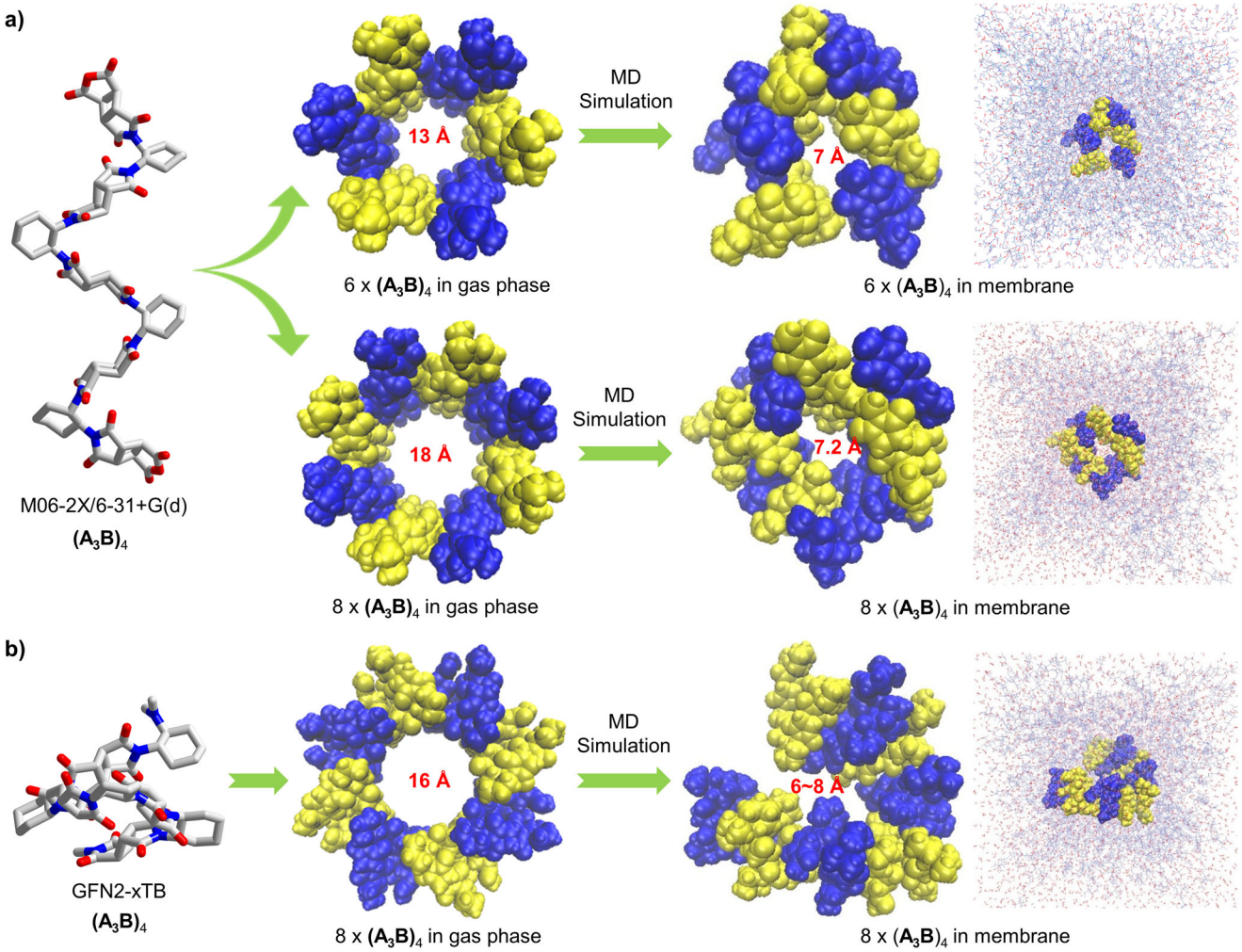

Figure 4. Computationally optimized structures of $(\mathbf{A_3B})_4$ in the gas phase and in lipid membrane. a) DFT-optimized structure of $(\mathbf{A_3B})_4$ at the M06-2X/6-31+G(d) level and its MD-simulated structures of hexameric and octameric ensembles after 200 ns simulation. b) Semi-empirical method-derived $(\mathbf{A_3B})_4$ at the GFN2-xTB level and its MD-simulated octameric ensemble after 200 ns simulation. For clarity of view, phospholipid and water molecules are omitted, and do note that these multimeric ensembles may involve the $(\mathbf{A_3B})_4$ segments from one or more polymer molecules.

have been reported.[60–66] Similarly, based on the experimental observation that polymer channels **2a** or **2b** efficiently transport Cl^- but not cations, we hypothesize that multiple $(\mathbf{A_3B})_4$ units may self-assemble within the lipid membrane via side chain-side chain interactions to generate barrel-like structures, thereby creating transmembrane channels for Cl^- transport (Figures 4 and S13). Although accurately resolving the atomic structure and formation mechanism of such transmembrane pores remains a significant challenge for both experimental and computational studies, we have conducted some preliminary investigations into the assembly behavior of multiple $(\mathbf{A_3B})_4$ units within lipid membranes.

We first identified the most stable $(\mathbf{A_3B})_4$ conformer using DFT calculations at the M06-2X/6-31+G(d) level and conformational sampling of over 70 candidates using the GFN2-xTB method. Subsequently, barrel-like models comprising five to eight $(\mathbf{A_3B})_4$ units were constructed and embedded within a DOPC lipid membrane for further molecular dynamics (MD) simulation.

For multimeric ensembles built from DFT-optimized $(\mathbf{A_3B})_4$ units, MD simulations reveal distinct assembly behaviors: While the pentameric and heptameric ensembles do not form well-defined central cavities (Figure S13a), both the hexameric and octameric assemblies adopt stable barrel-like structures, featuring a ~7 Å central cavity stabilized by side chain–side chain interactions (Figure 4a). For multimeric ensembles constructed from GFN2-xTB-sampled $(\mathbf{A_3B})_4$, partially enclosed cavities measuring approximately 12, 7–9, and 6–8 Å were observed in the hexameric, heptameric, and octameric forms, respectively (Figures 4b and S13b), with the cavity openings occupied by lipid molecules. These pores likely facilitate anion transport across the membrane by engaging the water O-atoms in the anion's hydration shell through their C–H groups, as supported by previous reports on pore-forming artificial membrane transporters.[60–66] Likewise, Barboiu et al. described a similar mechanism in which a net dipolar water wire along the pore surface forms hydrogen bonds with water molecules in the cation's hydration shell,

thereby promoting transmembrane transport of the hydrated cation.[69]

In conclusion, we developed a novel chiral polymer-based ion transport channel system using intrinsically microporous polyimides, demonstrating exceptional potential for advanced ion transport applications. The transport characteristics of these channels are intricately governed by the chiral configuration of the polymer monomers, resulting in distinct ion transport properties. The *cis*-diaminocyclohexane-derived chiral polymer achieves a record-breaking transport rate of 104 pS, representing unparalleled Li^+ transport activity. This surpasses all previously reported artificial Li^+ ion channels, while also exhibiting outstanding selectivity over Na^+ and K^+ ions. Conversely, the chiral polymers derived from *trans*-diaminocyclohexane display exceptional Cl^- transport performance, characterized by high conductance rates and a notable Cl^-/K^+ selectivity ratio of 17.6. This study highlights the innovative use of chiral polymers to construct ion transport channels with sharply contrasting properties dictated by their chirality. It introduces a transformative design paradigm for the development of next-generation polymer-based artificial ion channels.

Acknowledgements

The authors greatly appreciate the support of this work by the National Natural Science Foundation of China (22271049 and 22371048), the "Chu Ying Program" for the Top Young Talents of Fujian Province, the Postdoctoral Fellowship Program of CPSF under Grant Number GZC20230455, the Natural Science Foundation of Fujian Province (2023J01054), and a start-up grant from Fuzhou University.

Conflict of Interests

The authors declare no conflict of interest.

Data Availability Statement

The data that support the findings of this study are available from the corresponding author upon reasonable request.

Keywords: Artificial ion channels · Chiral induction · Chiral microporous polymers · Supramolecular chemistry · Transmembrane transport

[1] M. Mayer, J. Yang, *Acc. Chem. Res.* **2013**, *46*, 2998–3008.
[2] N. Sakai, S. Matile, *Langmuir* **2013**, *29*, 9031–9040.
[3] F. Otis, M. Auger, N. Voyer, *Acc. Chem. Res.* **2013**, *46*, 2934–2943.
[4] J. Montenegro, M. R. Ghadiri, J. R. Granja, *Acc. Chem. Res.* **2013**, *46*, 2955–2965.
[5] T. M. Fyles, *Acc. Chem. Res.* **2013**, *46*, 2847–2855.
[6] J.-Y. Chen, J.-L. Hou, *Org. Chem. Front.* **2018**, *5*, 1728–1736.
[7] H. Gill, M. R. Gokel, M. McKeever, S. Negin, M. B. Patel, S. Yin, G. W. Gokel, *Chem. Rev.* **2020**, *412*, 213264.
[8] S.-P. Zheng, L.-B. Huang, Z. Sun, M. Barboiu, *Angew. Chem. Int. Ed.* **2021**, *60*, 566–597.
[9] K. Sato, T. Muraoka, K. Kinbara, *Acc. Chem. Res.* **2021**, *54*, 3700–3709.
[10] J. Yang, G. Yu, J. L. Sessler, I. Shin, P. A. Gale, F. Huang, *Chem.* **2021**, *7*, 3256–3291.
[11] T. Yan, X. Zheng, S. Liu, Y. Zou, J. Liu, *Sci. China Chem.* **2022**, *65*, 1265–1278.
[12] A. Mondal, M. Ahmad, D. Mondal, P. Talukdar, *Chem. Commun.* **2023**, *59*, 1917–1938.
[13] L. He, T. Zhang, C. Zhu, T. Yan, J. Liu, *Chem. Eur. J.* **2023**, *29*, e202300044.
[14] M. Ahmad, S. A. Gartland, M. J. Langton, *Angew. Chem. Int. Ed.* **2023**, *62*, e202308842.
[15] J. Shen, C. Ren, H. Q. Zeng, *Acc. Chem. Res.* **2022**, *55*, 1148–1159.
[16] T. G. Johnson, M. J. Langton, *J. Am. Chem. Soc.* **2023**, *145*, 27167–27184.
[17] X. Yuan, J. Shen, H. Q. Zeng, *Chem. Commun.* **2024**, *60*, 482–500.
[18] D. Zhang, W. Chang, J. Shen, H. Q. Zeng, *Chem. Commun.* **2024**, *60*, 13468–13491
[19] J. J. Kasianowicz, *Chem. Rev.* **2012**, *112*, 6215–6217.
[20] T. J. Jentsch, K. Steinmeyer, G. Schwarz, *Nature* **1990**, *348*, 510–514.
[21] K. Steinmeyer, C. Ortland, T. J. Jentsch, *Nature* **1991**, *354*, 301–304.
[22] E. Gouaux, R. MacKinnon, *Science* **2005**, *310*, 1461–1465.
[23] K. S. Thorneloe, M. T. Nelson, *Can. J. Physiol. Pharm.* **2005**, *83*, 215–242.
[24] L. Wang, T.-M. Fu, Y. Zhou, S. Xia, A. Greka, H. Wu, *Science* **2018**, *362*, eaav4809.
[25] T. Jiang, A. Hall, M. Eres, Z. Hemmatian, B. Qiao, Y. Zhou, Z. Ruan, A. D. Couse, W. T. Heller, H. Huang, M. O. de la Cruz, M. Rolandi, T. Xu, *Nature* **2020**, *577*, 216–220.
[26] T. Yan, S. Liu, C. Li, J. Xu, S. Yu, T. Wang, H. Sun, J. Liu, *Angew. Chem. Int. Ed.* **2022**, *61*, e202210214.
[27] C. Li, Y. Wu, Y. Zhu, J. Yan, S. Liu, J. Xu, S. Fa, T. Yan, D. Zhu, Y. Yan, J. Liu, *Adv. Mater.* **2024**, *36*, 2312352.
[28] Y. Y. Lin, B. Wu, Y. Zeng, H. X. Yuan, C. X. Ji, Z. Q. Liu, Y. Sui, T. T. Yin, X. Kong, Y. T. Zhu, J. Chen, C. Lang, *Angew. Chem. Int. Ed.* **2024**, *63*, e202408558.
[29] C. Lang, W. Li, Z. Dong, X. Zhang, F. Yang, B. Yang, X. Deng, C. Zhang, J. Xu, J. Liu, *Angew. Chem. Int. Ed.* **2016**, *55*, 9723–9727.
[30] F. Chen, J. Shen, N. Li, A. Roy, R. J. Ye, C. L. Ren, H. Q. Zeng, *Angew. Chem. Int. Ed.* **2020**, *59*, 1440–1444.
[31] A. Roy, H. Joshi, R. J. Ye, J. Shen, F. Chen, *Angew. Chem. Int. Ed.* **2020**, *59*, 4806–4813.
[32] C. Zhang, J. Tian, S. Qi, B. Yang, Z. Dong, *Nano Lett.* **2020**, *20*, 3627–3632.
[33] J. Shen, J. Fan, R. J. Ye, N. Li, Y. Mu, H. Q. Zeng, *Angew. Chem. Int. Ed.* **2020**, *59*, 13328–13334.
[34] S. Qi, J. Tian, J. Zhang, L. Zhang, C. Zhang, Z. Lin, J. Min, S. Mao, Z. Dong, *CCS Chem.* **2022**, *4*, 1850–1857.
[35] J. Shen, R. Ye, Z. Liu, H. Q. Zeng, *Angew. Chem. Int. Ed.* **2022**, *61*, e202200259.
[36] J. Shen, Y. Li, Z. Li, H. Oh, H. Behera, H. Joshi, M. Kumar, A. Aksimentiev, H. Q. Zeng, *Angew. Chem. Int. Ed.* **2023**, *62*, e202305623.
[37] A. Roy, H. Joshi, J. Shen, W. Song, Y.-M. Tu, R. Chowdhury, R. Ye, N. Li, C. Ren, M. Kumar, A. Aksimentiev, H. Q. Zeng, *Nat. Nanotech.* **2021**, *16*, 911–917.
[38] J. Shen, A. Roy, H. Joshi, L. Samineni, R. J. Ye, Y.-M. Tu, W. Song, M. Skiles, M. Kumar, A. Aksimentiev, H. Q. Zeng, *Nano Lett.* **2022**, *22*, 4831–4838.
[39] F. Gou, Q. Wang, Z. Yang, W. Chang, J. Shen, H. Q. Zeng, *Angew. Chem. Int. Ed.* **2024**, *64*, e202418304.

[40] N. B. McKeown, P. M. Budd, *Chem. Soc. Rev.* **2006**, *35*, 675.
[41] N. B. McKeown, *Sci. China Chem.* **2017**, *60*, 1023–1032.
[42] Y. Wang, X. Ma, B. S. Ghanem, F. Alghunaimi, I. Pinnau, Y. Han, *Mater. Today Nano* **2018**, *3*, 69–95.
[43] M. Usman, A. Ahmed, B. Yu, Q. H. Peng, Y. Q. Shen, H. L. Cong, *Eur. Polym. J.* **2019**, *120*, 109262.
[44] N. B. McKeown, *Polymer* **2020**, *202*, 122736.
[45] Z. G. Wang, D. Wang, S. X. Zhang, L. Hu, J. Jin, *Adv. Mater.* **2016**, *28*, 3399–3405.
[46] Z. X. Low, P. M. Budd, N. B. McKeown, D. A. Patterson, *Chem. Rev.* **2018**, *118*, 5871–5911.
[47] Z. Y. Liu, Y. Liu, W. L. Qiu, W. J. Koros, *Angew. Chem. Int. Ed.* **2020**, *59*, 14877–14883.
[48] Z. Y. Liu, W. L. Qiu, W. Y. Quan, W. J. Koros, *Nat. Mater.* **2023**, *22*, 109–116.
[49] N. Guillou, C. Livage, M. Drillon, G. Férey, *Angew. Chem. Int. Ed.* **2003**, *42*, 5314–5317.
[50] D. V. Soldatov, I. L. Moudrakovski, J. A. Ripmeester, *Angew. Chem. Int. Ed.* **2004**, *43*, 6308–6311.
[51] L. Tang, L. Shi, C. Bonneau, J. Sun, H. Yue, A. Ojuva, B.-L. Lee, M. Kritikos, R. G. Bell, Z. Bacsik, J. Mink, X. Zou, *Nat. Mater.* **2008**, *7*, 381–385.
[52] L. Gómez-Hortigüela, J. Pérez-Pariente, F. Corà, *Micropor. Mesopor. Mater.* **2012**, *155*, 14–15.
[53] D. N. Dybtsev, A. L. Nuzhdin, H. Chun, K. P. Bryliakov, E. P. Talsi, V. P. Fedin, K. Kim, *Angew. Chem. Int. Ed.* **2006**, *45*, 916–920.
[54] J. Zhang, S. M. Chen, T. Wu, P. Y. Feng, X. H. Bu, *J. Am. Chem. Soc.* **2008**, *130*, 12882–12883.
[55] H. C. Ma, J. Zou, X. T. Li, G. J. Chen, Y. B. Dong, *Chem. Eur. J.* **2020**, *26*, 13754–13770.
[56] M. Xue, B. Lie, S. L. Qiu, B. L. Chen, *Mater. Today* **2016**, *19*, 503–515.
[57] Y. Shinno, K. Iyoki, K. Ohara, Y. Yanaba, Y. Naraki, T. Okubo, T. Wakihara, *Angew. Chem. Int. Ed.* **2020**, *59*, 20099–20103.
[58] X. Ma, I. Pinnau, *Macromolecules* **2018**, *51*, 1069–1076.
[59] E. K. O'Shea, J. D. Klemm, P. S. Kim, T. Alber, *Science* **1991**, *254*, 539–544.
[60] J. E. Jones, V. Diemer, C. Adam, J. Raftery, R. E. Ruscoe, J. T. Sengel, M. I. Wallace, A. Bader, S. L. Cockroft, J. Clayden, S. J. Webb, *J. Am. Chem. Soc.* **2016**, *138*, 688–695.
[61] C. L. Ren, F. Zeng, J. Shen, F. Chen, A. Roy, S. Zhou, H. Ren, H. Q. Zeng, *J. Am. Chem. Soc.* **2018**, *140*, 8817–8826.
[62] F. Zeng, F. Liu, L. Yuan, S. Zhou, J. Shen, N. Li, H. Ren, H. Q. Zeng, *Org. Lett.* **2019**, *21*, 4826–4830.
[63] L. Yuan, J. Shen, R. J. Ye, F. Chen, H. Q. Zeng, *Chem. Commun.* **2019**, *55*, 4797–4800.
[64] A. D. Peters, S. Borsley, F. della Sala, D. F. Cairns-Gibson, M. Leoni-dou, J. Clayden, G. F. S. Whitehead, I. J. Vitórica-Yrezμbal, E. Takano, J. Burthem, S. L. Cockroft, S. J. Webb, *Chem. Sci.* **2020**, *11*, 7023–7030.
[65] C. Dutta, P. Krishnamurthy, D. Su, S. H. Yoo, G. W. Collie, M. Pasco, J. K. Marzinek, P. J. Bond, C. Verma, A. Grélard, A. Loquet, J. Li, M. Luo, M. Barboiu, G. Guichard, R. M. Kini, P. P. Kumar, *Chem.* **2023**, *9*, 2237–2254.
[66] S. W. Deng, Z. Y. Zhong, L. Yuan, H. Q. Zeng, *Molecules* **2024**, *29*, 1118.
[67] S. Rex, *Biophys. Chem.* **1996**, *58*, 75–85.
[68] B. Hille, *Ion Channels of Excitable Membranes*, 3rd ed., Sinauer Associates, Sunderland, MA **2001**, pp. 283–294.
[69] M. Barboiu, Y. Le Duc, A. Gilles, P.-A. Cazade, M. Michau, Y. Marie Legrand, A. van der Lee, B. Coasne, P. Parvizi, J. Post, T. Fyles, *Nat. Commun.* **2014**, *5*, 4142.

Manuscript received: July 29, 2025
Revised manuscript received: September 02, 2025
Accepted manuscript online: September 03, 2025
Version of record online: ■■, ■■